PAPER

Construction of a double heterojunction between graphite carbon nitride and anatase TiO$_2$ with co-exposed (101) and (001) faces for enhanced photocatalytic degradation†

Jingjing Sun,‡[a] Lang Deng,‡[a] Jing Sun, [ID] *[a] Tingting Shen,*[a] Xikui Wang,[b] Rusong Zhao, [ID] [c] Yiyao Zhang[a] and Baolin Wang[a]

This study aimed to promote the separation of photogenerated carriers and improve the redox performance of graphite carbon nitride (g-C$_3$N$_4$) by synthesizing a double-heterojunction-structure photocatalyst, g-C$_3$N$_4$/(101)-(001)-TiO$_2$, through the solvothermal method. The photocatalyst comprised a Z-system formed from g-C$_3$N$_4$ and the (101) plane of TiO$_2$, as well as a surface heterojunction formed from the (101) and (001) planes of TiO$_2$. The results showed that g-C$_3$N$_4$/(101)-(001)-TiO$_2$ had strong photocatalytic activity and stable performance in the photodegradation of paracetamol. The active species ·O$_2^-$ and ·OH were found to play important roles in the photocatalytic degradation of paracetamol through a radical-quenching experiment. The charge-transfer mechanism was also described in detail. Overall, this work provided a new strategy for the Z-system heterojunction and opened up the application of this structure in the degradation of organic pollutants.

1. Introduction

Increased research attention is being paid to the environmental correlation between drugs from the chemical industry and hospitals and those used by humans and animals in the aquatic environment.[1] Take paracetamol, also known as 4-acetaminophen, which is a very common over-the-counter pain and fever reliever.[2] Given its high solubility and hydrophilicity, it easily accumulates in aqueous environments.[3] Even if the acetaminophen concentration detected in an aquatic environment is within the range of nanograms to micrograms per liter, the possibility of adverse effects on aquatic organisms and humans cannot be ruled out. These effects include acute and chronic damage, accumulation in tissues, reproductive damage, and inhibition of cell proliferation.[4,5] To avoid further accumulation of paracetamol in aquatic environments, the treatment of paracetamol wastewater should be given more attention. Advanced

oxidation processes such as heterogeneous photocatalysis, Fenton and photo-Fenton oxidation, ozonation, and UV/H$_2$O$_2$ are extensively used to treat many refractory organic compounds.[6] Considering that semiconductor-photocatalysis technology driven by solar energy has the advantages of low cost, effective degradation of pollutants, no secondary pollution, and ability to deal with environmental problems and lack of resources, this technology is widely applied.

Many studies have shown that graphite carbon nitride (g-C$_3$N$_4$) with a narrow band gap is an ideal photocatalyst. It has the advantages of no heavy metals, good chemical and thermal stabilities, easy preparation, low synthesis cost, and sensitivity to visible light.[7] Therefore, it is extensively used in photocatalytic hydrogen evolution, CO$_2$ reduction, and degradation of toxic organic pollutants.[8–10] However, pure g-C$_3$N$_4$ material cannot achieve an ideal visible-light response and has the disadvantages of relatively small specific surface area, fast recombination speed of photoelectron–hole pairs, and poor electron conductivity, which limit its photocatalytic performance.[11] To improve the catalytic activity of g-C$_3$N$_4$, researchers continue to attempt g-C$_3$N$_4$ modification.[12–15]

Among many photocatalysts, TiO$_2$ is believed to be a eligible candidate for forming a heterojunction with g-C$_3$N$_4$ due to their matching band-edge position.[16] The (101) and (001) planes of TiO$_2$ reportedly have strong reduction and oxidation properties, respectively. One of the issues regarding the difference in properties between the two (101) and (001) planes of TiO$_2$ has been discussed by researchers as reported in the literature.

[a]School of Environmental Science and Engineering, Qilu University of Technology (Shandong Academy of Sciences), Jinan 250353, PR China. E-mail: sunjing77@qlu.edu.cn; shentingting@qlu.edu.cn

[b]College of Environmental Science and Engineering, Shandong Agriculture and Engineering University, Jinan 251100, PR China

[c]College of c Key Laboratory for Applied Technology of Sophisticated Analytical Instrument of Shandong Province, Shandong Analysis and Test Center, Qilu University of Technology (Shandong Academy of Science), Jinan 250014, PR China

‡ These authors contributed equally to the work.

Using theoretical and experimental studies, Yang *et al.* showed that the (001) plane of anatase TiO_2 is more active than the thermodynamically stable (101) plane due to its higher surface energy.[17] In Han *et al.*'s experiments, methyl orange (MO) was used as a probe molecule to study the photocatalytic properties, showing that the (001) surface exhibited higher photocatalytic activity than the (101) surface due to the high density of active unsaturated titanium atoms and active surface oxygen atoms on the (001) surface.[18] When the two crystal planes are exposed at the same time, a surface heterojunction that can effectively inhibit the photogenerated electron–hole recombination forms between them and enhances the photocatalytic performance of anatase TiO_2.[19] Liang *et al.*[20] used hydrothermal and calcination methods to connect $g-C_3N_4$ and the (001) surfaces of to form two type-II heterojunctions. The formation of the heterojunction causes the catalyst to have a narrow band gap and to exhibit obvious visible-light absorption. Similarly, Zhang *et al.*[21] connected $g-C_3N_4$ with the (001) plane of TiO_2 to synthesize 2D/2D $g-C_3N_4/TiO_2$ nanosheets with a large area through solvent evaporation. However, the difference is that the photocatalytic system follows the charge-transfer mechanism of the Z-system. The electrons of TiO_2 could directly transfer to the valence band with $g-C_3N_4$ and recombine with the remaining holes, thereby achieving the purpose of photogenerated charge separation. In the above two studies, a $g-C_3N_4/TiO_2$ photocatalytic system is designed, and the active groups $\cdot O_2^-$ and h^+ play crucial roles in the system. The activity of the photocatalytic system varies with the transport path of the photogenerated carrier. Given that the $g-C_3N_4$ and (001) plane contained in TiO_2 can form a single or double-heterojunction structure, whether $g-C_3N_4$ forms a double-heterojunction structure with the (101) surface of (001)-(101)-TiO_2 to completely utilize the photogenerated electron–holes and improve the photocatalytic performance remains unknown.

In order to compound the two particles in different morphologies, various compounding methods have been tried by previous authors.[22,23] According to the literature, $g-C_3N_4/TiO_2$ photocatalysts have been synthesized by hydrothermal reaction method, sol–gel method, and soft template synthesis method, *etc*[24-26].

Li *et al.* synthesized $g-C_3N_4/TiO_2$ hybrid photocatalysts by changing the weight ratio of $g-C_3N_4$ under facile conditions by a modified sol–gel technique.[26] The results showed that heterojunctions were formed between $g-C_3N_4$ and TiO_2, and TiO_2 nanoparticles were well dispersed on the $g-C_3N_4$ sheets. Compared with pure $g-C_3N_4$ and TiO_2, the $g-C_3N_4/TiO_2$-80% hybrid photocatalyst exhibited stronger visible light photoactivity. The enhancement of the $g-C_3N_4/TiO_2$ hybrid photocatalyst can be attributed to its relatively high adsorption capacity and effective separation of photogenerated electron–hole pairs. Fu *et al.* successfully prepared $g-C_3N_4/TiO_2$ nanocomposites by a solid-state method using urea and TiO_2 as precursors, which exhibited enhanced absorption and photocatalytic properties in the visible region.[27]

In the present study, we prepared a double heterojunction of anatase TiO_2 with co-exposed (101) and (001) faces [(101)-(001)-TiO_2] and $g-C_3N_4$ through the solvothermal method. In this

composite, $g-C_3N_4$ was closely connected with the (101) plane of TiO_2 to form a Z-system heterojunction. Due to the synergistic effect between the Z-system heterojunction and the surface heterojunction of (101)-(001)-TiO_2, the separation of photogenerated carriers and the photocatalytic activity were improved. A possible charge-transfer mechanism on the double heterojunction for the enhancement in photocatalytic activity of $g-C_3N_4/(101)-(001)-TiO_2$ composite was also proposed. The *in situ* synthesis method has two advantages over traditional synthesis methods: (i) the formation process of the composite can be accurately controlled and followed. (ii) The relative content of the two materials can be easily controlled, which provides the possibility to obtain the microstructure clearly.[28]

2. Experimental methods

2.1 Experimental materials

The chemical reagents used in this experiment were analytically pure and there was no further treatment and purification. Commercial P25, urea, tetrabutyl titanate ($C_{16}H_{36}O_4Ti$), hydrofluoric acid (HF) and ethyl alcohol (EtOH) were purchased from China National Pharmaceutical Group Chemical Reagent Co., Ltd. Paracetamol and methylene blue (MB) were purchased from Shanghai Aladdin biochemical Technology Co., Ltd. The water solvent used in the whole experiment was deionized water.

2.2 Preparation of photocatalyst

2.2.1 Preparation of $g-C_3N_4$. $g-C_3N_4$ was prepared by simple calcination.[29] Simply, put 50 g urea into a porcelain crucible with a lid, place it in a blast drying box until the urea is completely dry, and then move it to a muffle furnace. At the heating rate of $5\,°C\,min^{-1}$, the temperature was raised to $550\,°C$ and kept for 3 h. Finally, the yellowish $g-C_3N_4$ powder was obtained.

2.2.2 Preparation of $g-C_3N_4/(101)-(001)-TiO_2$ composites. $g-C_3N_4/(101)-(001)-TiO_2$ composites were synthesized *in situ* by solvothermal method. Firstly, 1.15 g of $g-C_3N_4$ powder was added to the polytetrafluoroethylene lining with the capacity of 100 mL containing 30 mL ethyl alcohol and stirred continuously for 1 h until the solution was evenly mixed. Secondly, the 2.5 mL of $C_{16}H_{36}O_4Ti$ solution and 0.3 mL of HF (40%) was slowly added to the above solution and continued to stir 30 min. Then the autoclave was transferred to the blast drying box and heated continuously at $180\,°C$ for 12 h.[30] After the sample was cooled to room temperature, it was centrifuged and washed with ethyl alcohol and deionized water, and then dried to collect solids. Finally, the solids were ground to powder and put in a crucible with a lid and placed in the muffle furnace. The final sample was obtained by annealing at a heating rate of $5°C\,min^{-1}$, rising to $550\,°C$ and holding for 2 h. The purpose of annealing was to remove organic matter and F ions from the sample. At the same time, different proportions of $g-C_3N_4/(101)-(001)-TiO_2$-$x$ composites were prepared by changing the amount of $g-C_3N_4$ powder ($x = 1:2, 1:1, 2:1$ and $3:1$). Pure (101)-(001)-TiO_2 was prepared without adding $g-C_3N_4$, other conditions were the
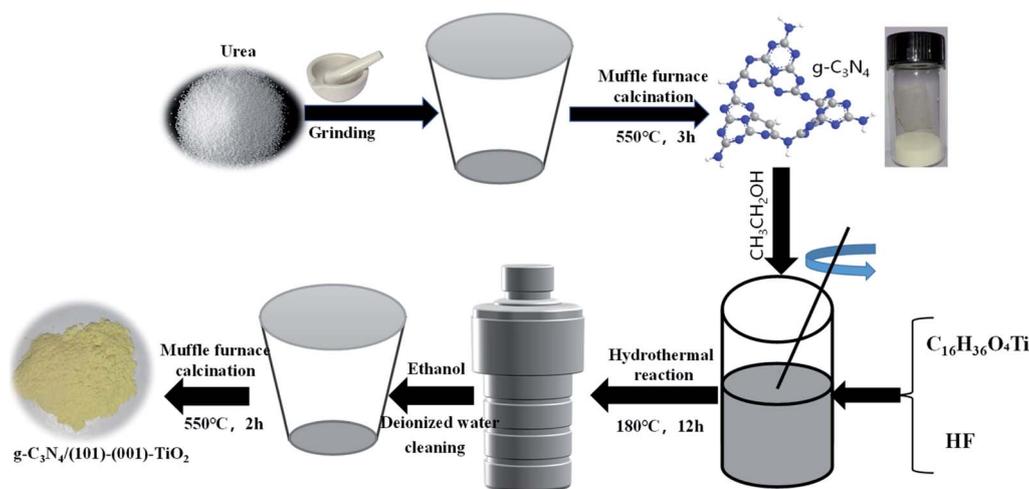
Scheme 1 Schematic diagram of the g-C$_3$N$_4$/(101)-(001)-TiO$_2$ photocatalysts fabrication process.

same. The preparation method of g-C$_3$N$_4$/P25 was placed in the ESI.†[30] Synthesis process of g-C$_3$N$_4$/(101)-(001)-TiO$_2$ photocatalyst in Scheme 1.

2.3 Characterization analysis

The crystal structure and crystallinity of the samples were characterized by X-ray diffraction (XRD D8 ADVANCE). Using Cu-Kα as the radiation source, the measuring angle 2θ was 5–80°. The molecular structure and chemical groups of the samples were analyzed by infrared spectroscopy (IR Affinity1s). The test method is KBr pressing method, with air as the background, and the scanning range is 500–4000 cm^{-1}. The morphology, crystal plane and lattice of the samples were characterized by transmission electron microscope (TEM) and high resolution transmission electron microscope (HRTEM, JEM-2100). The voltage of electron laser beam was 200 kV. X-ray photoelectron spectroscopy (XPS, Thermo ESCALAB 250Xi) was used to analyze the element composition and chemical valence on the surface of the sample. Ultraviolet-visible spectrophotometer (UV-Vis DRS, UV-2550) was used to analyze the optical absorption properties and reaction range of the samples. And the barium sulfate (BaSO$_4$) was used as the reference, and the scanning range was 300–600 nm. Electron spin resonance spectrometer (ESR, Bruker A300) was used to prove that the photocatalyst could produce active free radicals after illumination. The photocatalysts were irradiated with 300 W xenon lamp, and the free radicals were detected by adding traps.

2.4 Photocatalytic performance study

2.4.1 Photocatalytic activity experiment. In this experiment, paracetamol was used as the target pollutant to evaluate the photocatalytic performance of the composite photocatalyst under simulated solar radiation. For photocatalysts, the mass transfer process of pollutants reaching the catalyst surface may be limited, which results in lower photocatalytic efficiency. To solve this problem, the prepared g-C$_3$N$_4$/(101)-(001)-TiO$_2$ photocatalytic

material was well ground. The milled photocatalysts were placed in suspension and dispersed in the reaction system as a way to perform photocatalytic degradation. The specific operation steps are as follows: 0.1 g of the composite material was added to the paracetamol or MB solution of 10 ppm of 100 mL, and the solution was adsorbed by magnetic stirring for 1 h in the dark, so that the solution reached the adsorption–desorption equilibrium. The main purpose of this experiment is to exclude the interference of adsorption properties during the photocatalytic degradation of pollutants. After that, under the condition of magnetic stirring, it was irradiated under the light source of 300 W xenon lamp, which was equipped with a UV filter ($\lambda > 400$ nm). A certain amount of solution was extracted every hour and filtered by 0.22 µm filter membrane. And then the experimental data were determined and analyzed by high performance liquid chromatography (HPLC, LC-20A, Shimadzu, Japan). The main detection conditions were as follows: the type of chromatographic column was InertSustain C18 (4.6 × 250 mm); the mobile phase was composed of methanol and water (35 : 65, v/v) and the flow rate was 0.8 mL min^{-1}; the detection wavelength was 245 nm; the analysis time was 15 min; the column temperature was 35 °C and the injection volume was 5 µL. The concentration of MB was measured at 664 nm using a visible spectrophotometers (722N, Shanghai Precision & Scientific Instrument Co., Ltd.).

2.4.2 Active free radical capture experiment. In the photocatalytic reaction, in order to determine the active species that play crucial roles in the photocatalytic degradation process, hole trapping agent or free radical trapping agent was usually added to the photocatalytic reaction system. In this experiment, EDTA-2Na was used as the inhibitor of hole (h$^+$), *p*-benzoquinone (BQ) was used as the inhibitor of superoxide radical ($\cdot$O$_2$$^-$), and isopropanol (IPA) was used as the inhibitor of hydroxyl radical ($\cdot$OH). The dosage of capture agent was 2 mM, 0.01 g and 10 mM, respectively. Before avoiding light adsorption, the above trapping agents were added to the reaction system, and the other steps were the same as 2.4.1, from which

© 2022 The Author(s). Published by the Royal Society of Chemistry

the types of active free radicals in the process of photocatalytic degradation of paracetamol were determined.

3.   Results and discussion

3.1   X-ray diffraction (XRD) analysis

The XRD patterns of g-C_3N_4, (101)-(001)-TiO_2 and different proportions of g-C_3N_4/(101)-(001)-TiO_2 analyzed by X-ray diffractometer are shown in Fig. 1. Fig. 1(a) shows that two typical diffraction peaks of g-C_3N_4 were observed near $2\theta = 27.5°$ and 13.1°, corresponding to the (002) and (100) planes of g-C_3N_4, respectively.[31] Consistent with the standard data of g-C_3N_4 (JCPDS No. 87-1526).[32] The diffraction peaks of (101)-(001)-TiO_2 at 25.3°, 37.8°, 48.0°, 53.9°, 55.1°, and 62.7° corresponded to the crystal planes of anatase TiO_2 (PDF#84-1285).[17] The diffraction peaks of g-C_3N_4/(101)-(001)-TiO_2 composites with different ratios were similar to those of pure anatase (101)-(001)-TiO_2, but no characteristic peak of pure g-C_3N_4 was observed, which was primarily due to the poor crystallinity of g-C_3N_4, and the relatively small amount of g-C_3N_4 in g-C_3N_4/(101)-(001)-TiO_2 heterojunctions.[33,34] In addition, no other diffraction peaks were found in the diffraction pattern of the composite photocatalysts, indicating that the synthesized composites had high purity and did not produce other by-products. Fig. 1(b) is an enlarged image of the virtual box in Fig. 1(a). Compared with pure anatase (101)-(001)-TiO_2, with increased g-C_3N_4 addition, the diffraction peak intensity of the composites weakened and the broadening degree enlarged.

Notably, the diffraction peak of g-C_3N_4/(101)-(001)-TiO_2 composites moved to a higher diffraction angle by about 0.3° and 0.1°. The possible reason is the replacement of Ti^{4+} by C^{4+} of g-C_3N_4. The interlayer distance of g-C_3N_4/(101)-(001)-TiO_2 composites is reduced according to the Bragg equation $2d \sin\theta = n\lambda$.[35] In summary, a strong interaction existed between g-C_3N_4 and (101)-(001)-TiO_2.

3.2   Infrared (IR) analysis

The molecular structure and chemical groups of the samples were analyzed by IR spectroscopy, and the results are shown in Fig. 2. For (101)-(001)-TiO_2, it had a wide peak near 500 cm^{-1}, which was primarily attributed to the stretching vibration of Ti–O–Ti and Ti–O.[36] The sharp characteristic peak in 1631 cm^{-1} corresponded to the bending vibration of O–H in the H_2O molecule. g-C_3N_4 had two main IR broad peaks. The characteristic peak at 1200–1650 cm^{-1} was the typical stretching vibration of the C–N heterocycle, the characteristic peak at 1635 cm^{-1} was the stretching vibration mode of sp^2 C=N, and the characteristic peaks at 1244, 1408, and 1568 cm^{-1} corresponded to the stretching vibration of the aromatic sp3 C–N bond. The other absorption band was at 3000–3300 cm^{-1}, which corresponded to the stretching vibration mode of the terminal NH group. The characteristic peak at 809 cm^{-1} corresponded to the respiratory pattern of the triazine unit.[37,38] For different proportions of g-C_3N_4/(101)-(001)-TiO_2 hybrid materials, the main characteristic peaks of all hybrid materials were clearly seen, indicating that g-C_3N_4 and (101)-(001)-TiO_2 composite successfully formed. Notably, the absorption peak at 3300–

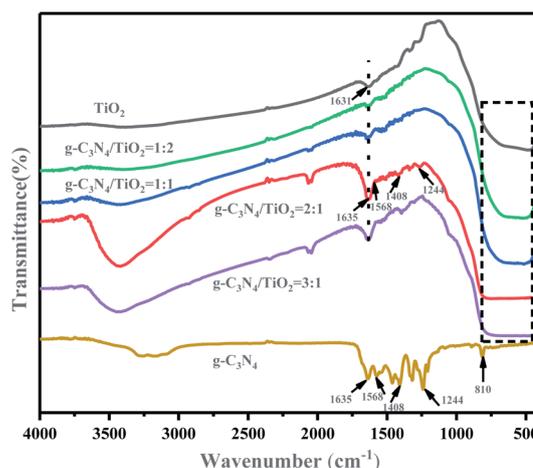Fig. 2   IR patterns of g-C_3N_4, (101)-(001)-TiO_2 and g-C_3N_4/(101)-(001)-TiO_2-x.

Fig. 1   XRD patterns of g-C_3N_4, (101)-(001)-TiO_2, and g-C_3N_4/(101)-(001)-TiO_2-x (a). Enlarged map of the dashed line (b).

3500 cm^{-1} corresponded to the stretching vibration of NH/OH,[20] indicating a large number of OH groups on the surface of g-C_3N_4/(101)-(001)-TiO_2, which benefited the photocatalytic redox reaction in contact with organic pollutants.

3.3 TEM and HRTEM analysis

The morphology and microstructure of individual and synthetized samples were characterized by TEM and HRTEM, and results are shown in Fig. 3. Fig. 3(a) shows a layered structure of g-C_3N_4, in which the middle layer may be stacked, indicating a flat graphite structure. Fig. 3(b) shows that (101)-(001)-TiO_2 nanocrystals had a typical truncated, octahedral, double-cone structure comprising eight isosceles trapezoidal (101) faces and two square (001) faces. The side length of the (001) face was 9.7 nm, which was also the upper side length of the (101) face, and the lower side length of the (101) face was 18.3 nm. It is calculated that the anatase TiO_2 nanocrystals contained 12.6% (001) faces and 87.4% (101) faces by using the equations[19] shown in the ESI.† Fig. 3(c) and (d) are the HRTEM images of (101)-(001)-TiO_2. It had crystal planes with lattice spacings of 0.224 and 0.3496 nm, which corresponded to the (001) and (101) faces of anatase TiO_2, respectively.[39] Fig. 3(e) and (f) show the image of g-C_3N_4/(101)-(001)-TiO_2, in which the g-C_3N_4 surface was found to be closely packed by nano-(101)-(001)-TiO_2, TiO_2 is

randomly distributed on the crushed multilayers of g-C_3N_4. This finding indicated a good combination of g-C_3N_4 and the (101) face of anatase TiO_2. Thus, the heterostructure formed on the surface of the two semiconductors was an ideal structure for accelerating charge transfer.[25,40] Based on the above analysis, we determined that the anatase TiO_2 in g-C_3N_4/(101)-(001)-TiO_2 samples had jointly exposed (001) and (101) crystal faces. The results of XRD, IR, and HRTEM analyses demonstrated that composites comprising g-C_3N_4 and (101)-(001)-TiO_2 were successfully prepared.

3.4 X-ray photoelectron spectroscopy (XPS) analysis

XPS was used to analyze the element composition and chemical valence on the surface of the samples. Fig. 4(a) shows the existence of C, O, and Ti in the g-C_3N_4/(101)-(001)-TiO_2 hybrid material. The intensity of the characteristic peak of C element weakened, and the N element basically disappeared. The possible reason was that (101)-(001)-TiO_2 completely covered the surface of g-C_3N_4. Notably, XPS analyzed the composition and chemical states of the composite surface, so C and N elements could not be detected to a great extent. This finding coincided with the results of XRD, IR, and TEM. The C 1s spectrum of g-C_3N_4 (Fig. S1(a)†) revealed that it had two main peaks at 284.8 eV (C–C) and 288.3 eV (N–C=N).[41] Thus, the

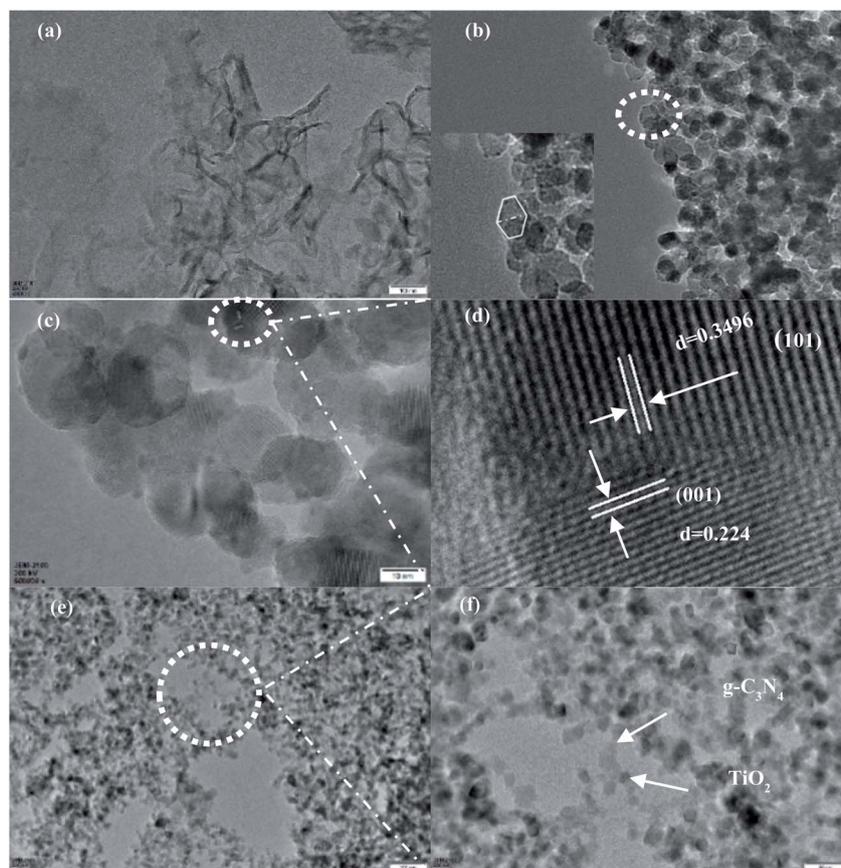**Fig. 3** TEM images of g-C_3N_4 (a), (101)-(001)-TiO_2 (b), and g-C_3N_4/(101)-(001)-TiO_2 (e). HRTEM images of (101)-(001)-TiO_2 (c). Images (d) and (f) are the enlarged portion of the dashed line in images (c) and (e), respectively.

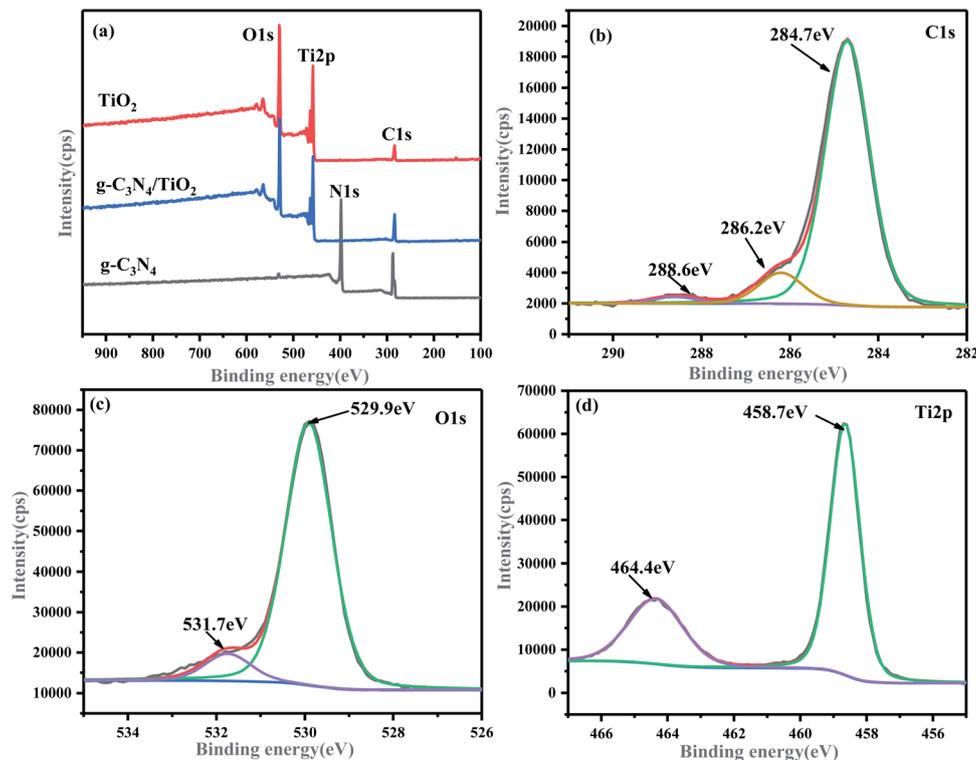**Fig. 4** XPS spectra of g-C_3N_4/(101)-(001)-TiO_2 hybrid material: survey spectra (a), C 1s spectra (b), O 1s spectra (c), and Ti 2p spectra (d).

recombination of g-C_3N_4 and (101)-(001)-TiO_2 affected the binding energy of C 1s, and the main peaks of C–C and N–C=N bonds shifted to 284.7 and 288.6 eV, respectively (Fig. 4(b)). The signal intensity of C–C weakened, indicating that the N and C species in g-C_3N_4 were active centers.[42]

At the same time, the characteristic peak of N–C (286.2 eV) was attributed to the existence of sp^2 hybrid carbon atoms with defects in the graphite structure.[43] Accordingly, the intensity of the N 1s main peak of the hybrid material g-C_3N_4/(101)-(001)-TiO_2 considerably weakened, as shown in Fig. S3.† Pure g-C_3N_4 showed three N 1s peaks at binding energies of 398.5, 399.0, and 400.5 eV, corresponding to C=N–C, N–C_3, and C–N–H, respectively (Fig. S1(b)†). However, when compounded with TiO_2, the binding energies of N–C_3 and C–N–H shifted to high binding energies of 399.4 and 401.0 eV, respectively. Therefore, the spectral line of Ti 2p of g-C_3N_4/(101)-(001)-TiO_2 shifted to the region of low binding energy (Fig. 4(d)). The main peaks of Ti $2p^{3/2}$ and Ti $2p^{1/2}$ of the composites were at 458.7 and 464.4 eV, respectively, whereas the main peaks of Ti $2p^{3/2}$ and Ti $2p^{1/2}$ of pure (101)-(001)-TiO_2 were at 458.8 and 464.5 eV, respectively (Fig. S2(b)†). Specific details of the peaks are given in Tables S1–S4.† The relatively low binding energy of Ti 2p and the relatively high binding energy of N 1s in the composite g-C_3N_4/(101)-(001)-TiO_2 were attributed to the transfer of electrons from Ti to N, proving a strong interaction between Ti and N.[19] The main characteristic peaks of C–O–Ti (529.9 eV) and N–C–O (531.7 eV) appeared in the O 1s spectrum of the hybrid material (Fig. 4(c)), indicating that oxidation occurred during the hydrothermal process and that g-C_3N_4/(101)-(001)-TiO_2 was successfully synthesized.[44] The results proves the successful synthesis of g-C_3N_4/(101)-(001)-TiO_2 heterojunction photocatalysts.

3.5 UV-vis DRS analysis

The spectra and bandgap widths of the samples obtained by UV-vis DRS analysis are shown in Fig. 5 and S4,† respectively. The band-gap widths of g-C_3N_4 and (101)-(001)-TiO_2 estimated by the Tauc plot method[45] were 2.69 and 3.0 eV, respectively (ESI, Fig. S4†). For (101)-(001)-TiO_2, it showed strong absorption within the wavelength range of $\lambda < 410$ nm, which well agreed
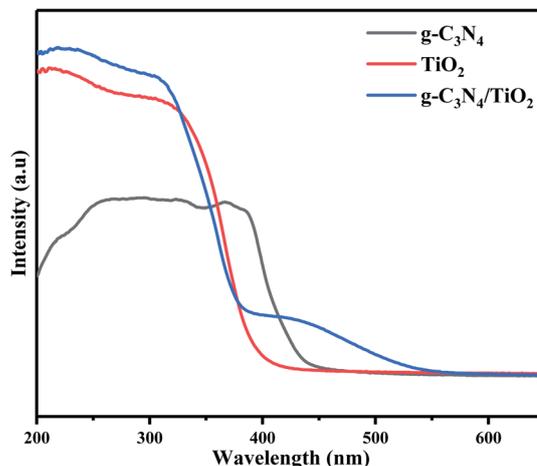
Fig. 5 UV-vis diffuse-reflectance spectra of the photocatalysts.

with the original band gap of anatase TiO_2. The band-gap absorption edge of g-C_3N_4 was about 460 nm, consistent with the intrinsic band gap of g-C_3N_4.[46] Compared with g-C_3N_4 and (101)-(001)-TiO_2, the absorption wavelength of the hybrid material red shifted. The modification of g-C_3N_4 by (101)-(001)-TiO_2 significantly influenced the broadening of the visible-light absorption range. Notably, the spectral curve of g-C_3N_4/(101)-(001)-TiO_2 hybrid material bulged and showed the most obvious red shift at 400 nm. This suggests that the g-C_3N_4/(101)-(001)-TiO_2 samples exhibit a better visible light response. It may be due to the synergistic effect between g-C_3N_4 and (101)-(001)-TiO_2 causing a change in the spatial structure, which in turn causes a red shift.[47]

Another reason may be the rearrangement of energy levels caused by the formation of chemical bonds (such as Ti–O–C and C–O–C covalent bond) between g-C_3N_4 and (101)-(001)-TiO_2, resulting in the redshift of the absorption-band edge.[48] Combining the UV-Vis DRS results with the above characterization results clearly indicates that the formation of the composites may be due to chemical bonding between the g-C_3N_4 and (101)-(001)-TiO_2 interfaces rather than a physical mixture of g-C_3N_4/(101)-(001)-TiO_2.

3.6 Analysis of photocatalytic performance

The photocatalytic activity of the composite photocatalysts with different ratios was investigated by the photocatalytic degradation of paracetamol solution under the irradiation of a 300 W xenon lamp ($\lambda > 420$ nm), simulating sunlight. As shown in Fig. 6, when the solution of paracetamol was irradiated directly with a xenon lamp in the absence of photocatalyst, almost no degradation of paracetamol solution occurred, indicating that paracetamol was stable under direct light and cannot be photodegraded. Moreover, the photocatalytic system formed by g-C_3N_4, (101)-(001)-TiO_2 and four groups of different-ratio g-C_3N_4/(101)-(001)-TiO_2 composites could all cause the degradation of paracetamol. When the content of g-C_3N_4 was twice that of (101)-(001)-TiO_2, the composite showed excellent photocatalytic

activity, and photodegradation efficiency reached 66.49% within 6 h (Fig. S5†). The photocatalytic degradation rate[37] of paracetamol by g-C_3N_4/(101)-(001)-TiO_2 = 2 : 1 was 0.1746 h^{-1}, which was 1.69 and 4.14 times higher than that of g-C_3N_4 and (101)-(001)-TiO_2, respectively (Table S5†). For comparison, MB was photocatalyzed by g-C_3N_4/(101)-(001)-TiO_2 and P25 at the same time, and the composite also showed strong photocatalytic performance (Fig. S6†). Moreover, after four repeated degradation experiments (Fig. 7(a)), the degradation effect of the catalyst on paracetamol was almost the same, indicating that the composite could be reused and had good light stability. This finding was also by the XRD patterns of the sample collected after cycle experiments (Fig. 7(b)).

On this basis, we explored the effects of HF amount in the preparation process, the solution pH, and interfering ions in the reaction system on photocatalytic activity. As a surface-control agent for crystal-surface growth, the addition amount of HF played an important role in influencing the exposure of the (001) surface of anatase TiO_2. A greater HF amount led to a greater proportion of exposed (001) surface. Consequently, the morphology of TiO_2 changed from octahedral bipyramid to nanoplates or nanosheets.[49] Fig. 8 shows that with increased HF

Fig. 7 Cyclic photocatalytic degradations of paracetamol in the presence of g-C_3N_4/(101)-(001)-TiO_2 = 2 : 1 (a). XRD patterns of the sample before and after the cycle experiments (b).
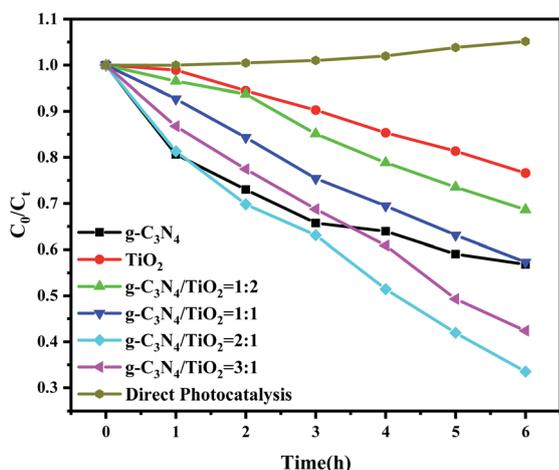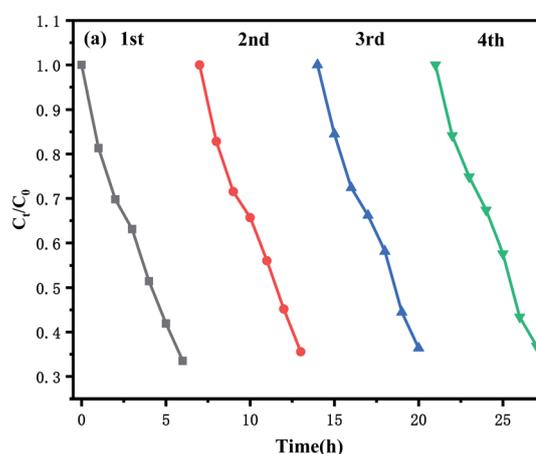

Fig. 6 Photocatalytic degradation of paracetamol by different photocatalysts under the irradiation of a 300 W xenon lamp ($\lambda > 420$ nm).
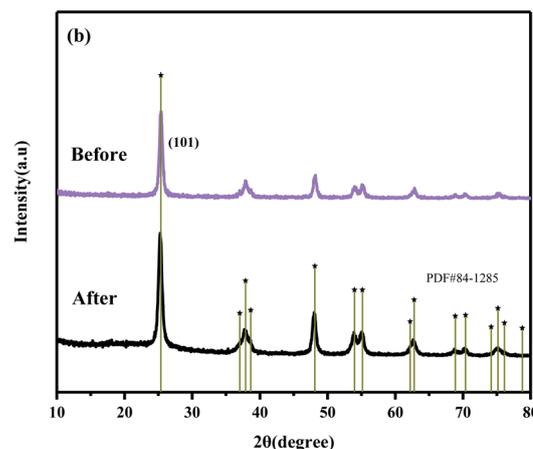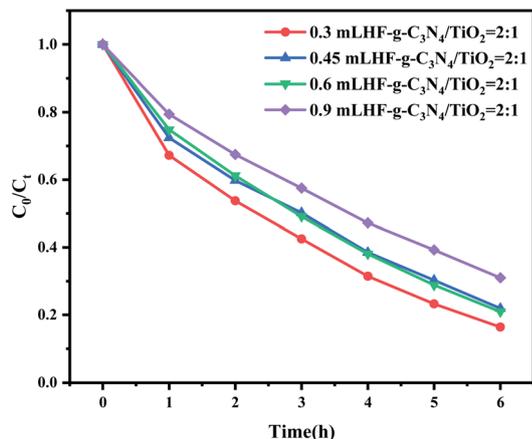
Fig. 8 Effect of HF dosage on the photocatalytic activity of the reaction system.

dosage, the photocatalytic degradation of paracetamol by g-C_3N_4/(101)-(001)-TiO_2 = 2 : 1 decreased. The increase in the (001) plane proportion led to decreased photocatalytic performance. Therefore, the heterostructure formed by g-C_3N_4 and anatase TiO_2 with a large ratio of (101) surface was more effective in degrading paracetamol.

In addition to paracetamol within the range of nanograms to micrograms per liter, many metal ions, inorganic nonmetal ions, and humus are present in aqueous environments. The aqueous pH and the presence of ions could also affect the reaction system. Fig. S7 and S8† show the effects of pH and interfering ions (humus, Cl^-, SO_4^{2-}, and NO_3^-), respectively. When the reaction solution is pH 7, g-C_3N_4/(101)-(001)-TiO_2 had the best degradation effect on paracetamol. The existence of humic acid, Cl^-, SO_4^{2-}, and NO_3^- also had a slight effect on the reaction system, but g-C_3N_4/(101)-(001)-TiO_2 still had a certain degradation effect on paracetamol, indicating that it could selectively degrade paracetamol molecules in solution during photocatalytic reaction.

3.7 Analysis of photocatalytic mechanism

To explore the catalytic mechanism of photocatalytic reaction, the main active species in g-C_3N_4, (101)-(001)-TiO_2, and g-C_3N_4/(101)-(001)-TiO_2 composite photocatalytic systems were detected by free radical-quenching experiments. Fig. 9(a) shows that different traps had various effects on paracetamol photodegradation. When BQ or IPA was used as a trapping agent, the photocatalytic-degradation efficiency of the three photocatalytic systems decreased significantly, and the inhibition effect of adding BQ became more obvious, indicating that $\cdot O_2^-$ and $\cdot OH$ were the main active species. In the presence of EDTA-2Na, the photodegradation efficiency of the (101)-(001)-TiO_2 photocatalysis system obviously decreased, whereas that of the g-C_3N_4/(101)-(001)-TiO_2 photocatalysis system did not decrease significantly. Meanwhile, the degradation efficiency of paracetamol by the g-C_3N_4 photocatalysis system increased. The possible reason for this phenomenon was that EDTA-2Na promoted the separation of photogenerated electron–hole pairs by capturing holes. The separated electrons transferred onto the catalyst surface and reacted with molecular oxygen to produce $\cdot O_2^-$. It was involved in the photocatalytic redox reaction of paracetamol, thereby improving the efficiency of photocatalytic degradation. In the composite photocatalytic system, the degradation efficiency of paracetamol was only slightly reduced due to the capture of h^+, indicating h^+ was not the main species for the photocatalytic degradation of paracetamol.

To prove the results obtained from the above capture experiments, the existence of $\cdot O_2^-$ and $\cdot OH$ free radicals was further confirmed by ESR, as shown in Fig. 9(b). No ESR signal was detected under dark conditions. After light irradiation for 10 min, six typical peaks of DMPO-$\cdot O_2^-$ and four characteristic peaks of DMPO-$\cdot OH$ could be clearly observed in the composite photocatalytic systems. The energy band of g-C_3N_4 and (101)-(001)-TiO_2 could be calculated by the following relations (1) and (2):
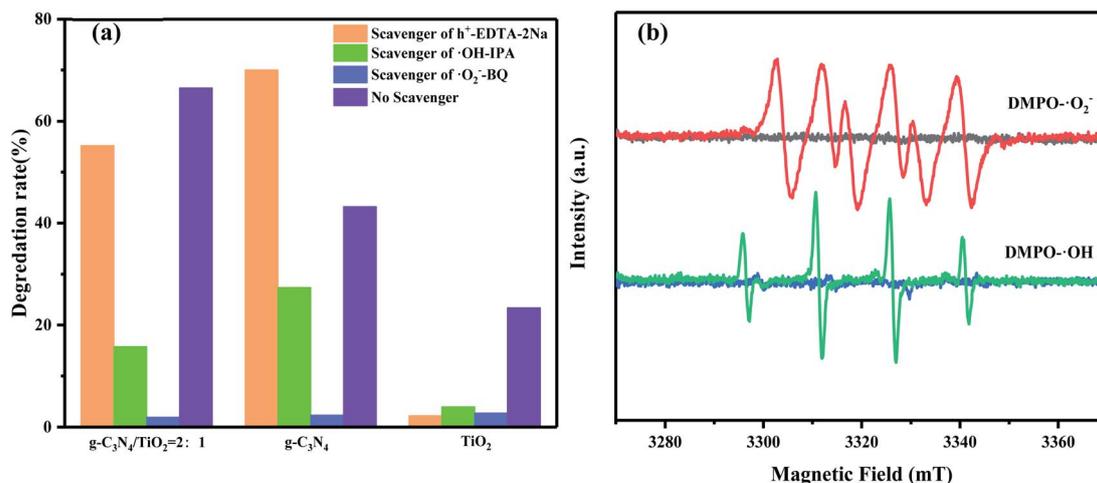
$$E_{VB} = \chi - E^e + 0.5E_g \tag{1}$$

Fig. 9 Effects of different capture agents on the photocatalytic degradation of paracetamol by different photocatalysts (a). ESR spectra of radical adducts trapped by DMPO in g-C_3N_4/(101)-(001)-TiO_2 dispersion as a function of time under dark and visible light (in methanol dispersion for DMPO-$\cdot O_2^-$ and in aqueous solution for DMPO-$\cdot OH$) (b).

$$E_{CB} = E_{VB} - E_g \qquad (2)$$

where E_{VB} and E_{CB} are the band-edge potentials of valence and conduction bands, respectively; E^e is the energy of free electrons with the hydrogen scale (~4.5 eV); χ is the absolute electronegativity of the semiconductor; and E_g is the band gap of semiconductor in electron volts.[50,51] In the present study, the highest E_{VB} and E_{CB} potentials of g-C_3N_4 (~2.69 eV) were 1.58 and −1.11 eV. The band gap of (101)-(001)-TiO_2 was ~3.0 eV, and the estimated E_{VB} and E_{CB} potentials were 2.18 and −0.82 eV, respectively. Yu *et al.* calculated the electronic structures of the (001) and (101) crystal planes by first-principles quantum chemistry, and the Fermi energy levels of the (001) planes enter their valence bands.[52] However, the Fermi energy level of the (101) face is still located at the top of the valence band of the (101) face. Since the (001) and (101) facets are in contact with each other, their Fermi energy levels should be equal. In this regard, the (001) and (101) surfaces can form a surface heterojunction, which facilitates the transfer and separation of photogenerated electrons and holes.[39,53] The percentage of exposed (001) and (101) surfaces reaches its optimum at an increase of 0.3 mL of HF amount. In this case, electron and hole pairs can efficiently migrate to the (101) and (001) surfaces, respectively. However, further increasing the number of (001) facets on the TiO_2 surface may lead to the effect of electron spillover to the (101) facets.[52]

Based on the above results, we proposed a possible reaction mechanism to explain the enhanced photocatalytic activity of the composites, as shown in Fig. 10. First, considering the surface heterostructure of (101)-(001)-TiO_2, the photogenerated electrons produced by the (001) plane of TiO_2 rapidly transferred to the (101) plane, and the photogenerated holes transferred to the (001) plane under visible-light irradiation. Second,

we inferred that the Z-type heterostructure formed on the g-C_3N_4 with the (101) plane of TiO_2, rather than with the (001) plane. On one hand, due to the valence-band energy level of g-C_3N_4 being more positive than that of (101)-(001)-TiO_2, the photogenerated hole was finally transferred to the valence band of g-C_3N_4. However, the E_{VB} value (1.58 eV *vs.* NHE) of g-C_3N_4 was lower than the standard redox potential (1.99 eV *vs.* NHE) of ·OH/OH⁻ and the standard redox potential (2.37 eV *vs.* NHE) of ·OH/H_2O, which did not produce ·OH radicals[54,55] (this point could be proven by Fig. S9†).

However, capture experiments and ESR results proved the existence of ·OH free radicals and its role as the main active group of the reaction system. The photogenerated holes generated by the (101) plane of TiO_2 transferred to the (001) plane and reacted with the adsorbed water to produce ·OH radicals. Therefore, the (101) surface of TiO_2 was loaded on g-C_3N_4. On the other hand, the conduction-band energy level of g-C_3N_4 was more negative than that of TiO_2, and the electrons produced by photoexcited g-C_3N_4 reacted more easily with molecular oxygen to form ·O_2^-. The electrons produced by TiO_2 remained on the conduction band of the (101) plane, and they recombined with the holes remaining in the g-C_3N_4 valence band, thereby promoting the separation of photogenerated carriers. In this case, the transfer pathway of photogenerated carriers on the heterojunction interface between the g-C_3N_4 and the (101) plane of TiO_2 followed the direct Z system. In summary, the composite of g-C_3N_4 and (101)-(001)-TiO_2 formed a double-heterojunction structure, *i.e.*, a surface heterostructure between the (101) and (001) surfaces of TiO_2 and a Z-type heterojunction between the g-C_3N_4 and (001) crystal surfaces, which accelerated the separation and transfer rate of photogenerated charges, enhanced the photocatalytic performance, and effectively degraded organic pollutants.
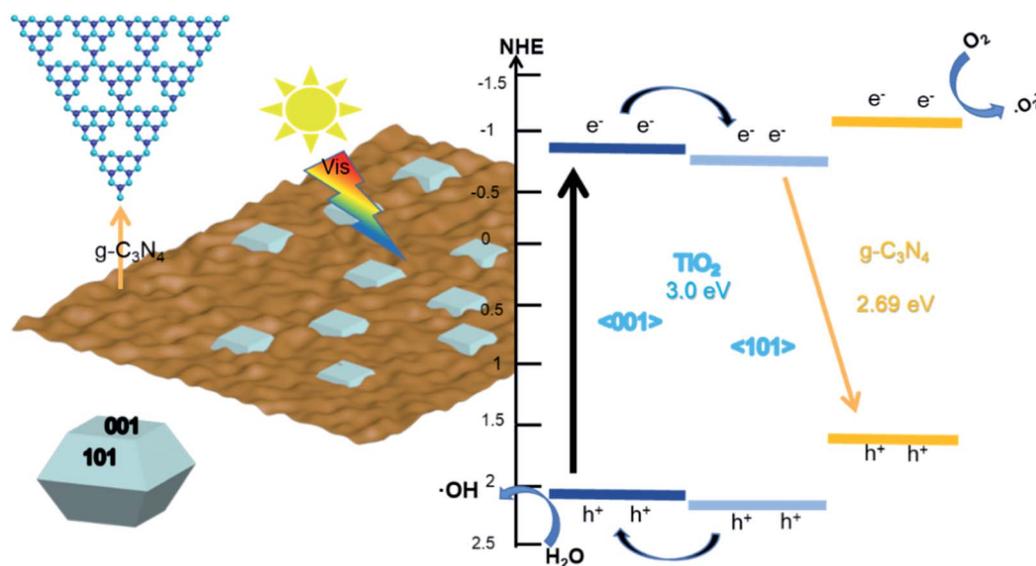

Fig. 10 Proposed bandgap structure and mechanism for the photodegradation of pollutant by g-C_3N_4/(101)-(001)-TiO_2 under visible-light irradiation.

4. Conclusion

g-C_3N_4 and anatase TiO_2 with co-exposed (101) and (001) planes formed a double heterojunction through the solvothermal method, that is, the Z-system formed by g-C_3N_4 and the (101) plane of TiO_2 and the surface heterojunction formed by the (101) and (001) planes. Under visible light irradiation, the g-C_3N_4/(101)-(001)-TiO_2 hybrid material showed good degradation activity for paracetamol with the reaction-rate constants 1.69 and 4.14 times higher than that of pure g-C_3N_4 and (101)-(001)-TiO_2, respectively. In the paracetamol photo-degradation process, $\cdot O_2^-$ and $\cdot OH$ were the main active species in the composite photocatalytic system. This point differed from those in other literature, in which the main active species in g-C_3N_4/TiO_2 system were $\cdot O_2^-$ and h^+. On this basis, a possible charge-transfer mechanism was proposed. Specifically, under visible-light irradiation, the electrons on the conduction band of the (001) plane of TiO_2 transferred to the (101) surface and finally recombined with the holes on the valence band of g-C_3N_4. The holes on the (101) plane then transferred to the (001) plane and reacted with the water molecules adsorbed on the surface of the material to produce $\cdot OH$. The photogenerated electrons produced by g-C_3N_4 directly reduced oxygen molecules to $\cdot O_2^-$. This double heterojunction promoted the separation of photo-generated carriers and enhanced the redox ability of g-C_3N_4/(101)-(001)-TiO_2. Overall, this work provided a new strategy for the development of a photocatalytic system with Z-system heterojunction to fulfill their potential in the degradation of organic pollutants.

Author contributions

Jingjing Sun: conceptualization, methodology, software, writing – original draft. Lang Deng: conceptualization, resources, methodology, writing – original draft. Jing Sun: resources, funding acquisition, formal analysis, supervision. Xikui Wang: project administration, investigation. Tingting Shen: funding acquisition, validation, data curation. Rusong Zhao: funding acquisition, supervision. Yiyao Zhang: visualization. Baolin Wang: funding acquisition, data curation.

Funding

Conflicts of interest

The authors declare no conflict of interest.

Notes and references

1 K. H. Langford and K. V. Thomas, *Environ. Int.*, 2009, **35**, 766–770.
2 J. R. Bales, J. K. Nicholson and P. J. Sadler, *Clin. Chem.*, 1985, **31**, 757–762.
3 M. J. Benotti, R. A. Trenholm, B. J. Vanderford, J. C. Holady and S. A. Snyder, *Environ. Sci. Technol.*, 2009, **43**, 597–603.
4 P. J. Phillips, S. G. Smith, D. W. Kolpin, S. D. Zaugg, H. T. Buxton, E. T. Furlong, K. Esposito and B. Stinson, *Environ. Sci. Technol.*, 2010, **44**, 4910–4916.
5 B. I. Escher, R. Baumgartner, M. Koller, K. Treyer, J. Lienert and C. S. McArdell, *Water Res.*, 2011, **45**, 75–92.
6 W. Silva, M. A. Lansarin, J. H. Z. D. Santos and F. Silveira, *Water Sci. Technol.*, 2016, **74**, 2370.
7 X. Wang, K. Maeda, A. Thomas, K. Takanabe, G. Xin, J. M. Carlsson, K. Domen and M. Antonietti, *Nat. Mater.*, 2009, **8**, 76–80.
8 Y. Wang, P. Wang and P. Antonietti, *Angew. Chem.*, 2012, **51**, 68–89.
9 J. Liu, L. Yang, N. Liu, Y. Han, Z. Xing, H. Huang, Y. Lifshitz, S. T. Lee, J. Zhong and Z. Kang, *Science*, 2015, **46**, 970–974.
10 D. Huang, X. Yan, Y. Ming, G. Zeng, C. Zhou, J. Wan, M. Cheng and W. Xue, *ACS Appl. Mater. Interfaces*, 2018, **10**, 21035–21055.
11 X. Wang, S. Blechert and M. Antonietti, *ACS Catal.*, 2012, **2**, 1596–1606.
12 X. Bi, S. Yu, E. Liu, L. Liu, K. Zhang, J. Zang and Y. Zhao, *Colloids Surf., A*, 2020, **603**, 125193.
13 N. Boonprakob, N. Wetchakun, S. Phanichphant, D. Waxler, P. Sherrell, A. Nattestad, J. Chen and B. Inceesungvorn, *J. Colloid Interface Sci.*, 2014, **417**, 402–409.
14 C. Murugan, K. Ranjithkumar and A. Pandikumar, *J. Colloid Interface Sci.*, 2021, **602**, 437–451.
15 C. Murugan, M. Karnan, M. Sathish and A. Pandikumar, *Catal. Sci. Technol.*, 2020, **10**, 2427–2442.
16 J. Sun, J. Sun and X. Wang, *Chem. - Asian J.*, 2020, **15**, 4168–4183.
17 H. G. Yang, C. H. Sun, S. Z. Qiao, J. Zou, G. Liu, S. C. Smith, H. M. Cheng and G. Q. Lu, *Nature*, 2008, **453**, 638–641.
18 X. Han, Q. Kuang, M. Jin, Z. Xie and L. Zheng, *J. Am. Chem. Soc.*, 2009, **131**, 3152–3153.
19 J. Yu, J. Low, W. Xiao, P. Zhou and M. J. Jaroniec, *J. Am. Chem. Soc.*, 2014, **136**, 8839–8842.
20 D. Liang, Y. Huang, F. Wu, J. Luo, X. Yi, J. Wang and X. Qiu, *Appl. Surf. Sci.*, 2019, **487**, 322–334.
21 X. Zhang, L. Li, Y. Zeng, F. Liu, J. Yuan, X. Li, Y. Yu, X. Zhu, Z. Xiong, H. Yu and Y. Xie, *ACS Appl. Nano Mater.*, 2019, **2**, 7255–7265.
22 S. Vinoth, W.-J. Ong and A. Pandikumar, *J. Colloid Interface Sci.*, 2021, **591**, 85–95.
23 S. Vinoth, P. M. Rajaitha and A. Pandikumar, *New J. Chem.*, 2021, **45**, 2010–2018.

24 C. Murugan, K. Bhojanaa, W.-J. Ong, K. Jothivenkatachalam and A. Pandikumar, *Int. J. Hydrogen Energy*, 2019, **44**, 30885–30898.

25 P. Mary Rajaitha, K. Shamsa, C. Murugan, K. Bhojanaa, S. Ravichandran, K. Jothivenkatachalam and A. Pandikumar, *SN Appl. Sci.*, 2020, **2**, 1–14.

26 C. Li, Z. Sun, Y. Xue, G. Yao and S. Zheng, *Adv. Powder Technol.*, 2016, **27**, 330–337.

27 M. Fu, J. Pi, F. Dong, Q. Duan and H. Guo, *Int. J. Photoenergy*, 2013, **2013**, 1–7.

28 K. Wang, B. Liu, J. Li, X. Liu, Y. Zhou, X. Zhang, X. Bi and X. Jiang, *J. Mater. Sci. Technol.*, 2019, **35**, 615–622.

29 Y. Zhang, J. Liu, W. Guan and W. Chen, *Nanoscale*, 2012, **4**, 5300–5303.

30 M. Ding, W. Wang, Y. Zhou, C. Lu, Y. Ni and Z. Xu, *J. Alloys Compd.*, 2015, **635**, 34–40.

31 F. Goettmann, A. Fischer, M. Antonietti and A. Thomas, *New J. Chem.*, 2007, **31**, 1455–1460.

32 D. Liang, Y. Huang, F. Wu, J. Luo, X. Yi, J. Wang and X. Qiu, *Appl. Surf. Sci.*, 2019, **487**, 322–334.

33 M. Huang, J. Yu, Q. Hu, W. Su, M. Fan, B. Li and L. Dong, *Appl. Surf. Sci.*, 2016, **389**, 1084–1093.

34 L. Gu, J. Wang, Z. Zou and X. Han, *J. Hazard. Mater.*, 2014, **268**, 216–223.

35 M. Huang, J. Yu, Q. Hu, W. Su, M. Fan, B. Li and L. Dong, *Appl. Surf. Sci.*, 2016, **389**, 1084–1093.

36 P. M. Martins, C. G. Ferreira, A. R. Silva, B. Magalhaes, M. M. Alves, L. Pereira, P. Marques, M. Melle-Franco and S. Lanceros-Mendez, *Composites, Part B*, 2018, **145**, 39–46.

37 H. F. Shi, G. Q. Chen, C. L. Zhang and Z. G. Zou, *ACS Catal.*, 2014, **4**, 3637–3643.

38 Y. Bo, J. Wei, T. Hu, H. Yao, Z. Jiang, Z. Fang and Z. Chu, *Chin. J. Catal.*, 2015, **36**, 1009–1016.

39 S. Liu, J. Yu and M. Jaroniec, *Chem. Mater.*, 2011, **23**, 4085–4093.

40 V. Selvaraj and A. Pandikumar, *J. Phys. Chem. C*, 2021, **126**, 79–90.

41 J. J. Wu, N. Li, X. H. Zhang, H. B. Fang, Y. Z. Zheng and X. Tao, *Appl. Catal., B*, 2018, **226**, 61–70.

42 W. Wang, J. Fang, S. Shao, M. Lai and C. Lu, *Appl. Catal., B*, 2017, **217**, 57–64.

43 L. Pan, X. D. Zhu, X. M. Xie and Y. T. Liu, *Adv. Funct. Mater.*, 2015, **25**, 3341–3350.

44 R. Hao, G. Wang, H. Tang, L. Sun and D. Han, *Appl. Catal., B*, 2016, **187**, 47–58.

45 Y. Feng, S. Lin, S. Huang, S. Shrestha and G. Conibeer, *J. Appl. Phys.*, 2015, **117**, 5447–5451.

46 X. Jian, G. Wang, J. Fan, B. Liu and J. Yu, *J. Power Sources*, 2015, **274**, 77–84.

47 P. Mary Rajaitha, K. Shamsa, C. Murugan, K. B. Bhojanaa, S. Ravichandran, K. Jothivenkatachalam and A. Pandikumar, *SN Appl. Sci.*, 2020, **2**, 572.

48 H. G. Yang, C. H. Sun, S. Z. Qiao, J. Zou, G. Liu, S. C. Smith, H. M. Cheng and G. Q. Lu, *Nature*, 2008, **453**, 638.

49 Z. He, L. Wen, W. Da, Y. Xue and S. J. Shuang, *Energy Fuels*, 2014, **28**, 3982–3993.

50 K. Dai, L. Lu, C. Liang, Q. Liu and G. Zhu, *Appl. Catal., B*, 2014, **156–157**, 331–340.

51 G. Li, X. Nie, J. Chen, Q. Jiang, T. An, P. K. Wong, H. Zhang, H. Zhao and H. Yamashita, *Water Res.*, 2015, **86**, 17–24.

52 J. Yu, J. Low, W. Xiao, P. Zhou and M. Jaroniec, *J. Am. Chem. Soc.*, 2014, **136**, 8839–8842.

53 Z. Zheng, B. Huang, J. Lu, X. Qin, X. Zhang and Y. Dai, *Chem. - Eur. J.*, 2011, **17**, 15032–15038.

54 Z. Jiang, W. Wan, H. Li, S. Yuan, H. Zhao and P. K. Wong, *Adv. Mater.*, 2018, **30**, 1706108.

55 D. Deng, Y. Hao, S. Yang, Q. Han, L. Liu, Y. Xiang, F. Tu and N. Xia, *Sens. Actuators, B*, 2019, **286**, 415–420.